

# A General Analytical Model of Permanent Magnet Eddy Current Couplings

Jian Wang<sup>1,2</sup>, Heyun Lin<sup>1</sup>, Shuhua Fang<sup>1</sup>, and Yunkai Huang<sup>1</sup>

<sup>1</sup>School of Electrical Engineering, Southeast University, Nanjing, Jiangsu 210096, China

<sup>2</sup>School of Automation, Nanjing Institute of Technology, Nanjing, Jiangsu 211167, China

An improved practical two-dimensional model for the analytical calculation of the magnetic field distributions in permanent magnet (PM) eddy current couplings is presented to obtain the torque characteristics. By establishing the Cartesian coordinate reference system on the rotating conductor, the PM region is treated as a source of traveling wave magnetic field and then the multi-layer boundary value problem is solved. The formulation for the magnet blocks, the eddy current and saturation effects in the solid secondary back iron, and the equivalence relationships between typical PM shapes, are all reasonably taken into account. Calculation results produced by the proposed analytical model are compared with those from the nonlinear finite element method and experimental measurement.

**Index Terms**—Coupling, eddy current, permanent magnet, saturation effect.

## I. INTRODUCTION

PERMANENT magnet (PM) eddy current couplings can transfer torque without any mechanical contact and wear. They offer the main benefits of efficient operation, vibration isolation, no maintenance, and seizure protection, and thus have been used in many industrial applications, such as blowers, pumps, conveyors and damping systems [1]–[4]. The transmitted torque, originating from the induced current in the conductor due to its motion relative to the PMs, can be flexibly changed by adjusting the air gap for axial flux couplings or by regulating the overlapping area between the magnets and the conductor for radial flux couplings. The typical axial flux and radial flux couplings are illustrated schematically in Fig. 1, where  $n_1$  and  $n_2$  are the rotation speeds of the primary and the secondary, respectively, and are all measured in rpm.

Such moving conductor eddy current problems containing ferromagnetic parts can be solved by using two-dimensional (2-D) or three-dimensional (3-D) numerical methods [1], [5], [6]. The numerical approaches, however, are commonly hampered by the convergence of iteration calculation and the computational stability for high-speed cases by reason of high Peclet numbers, especially for 3-D problems [7], [8]. A detailed description of the Peclet number will be given in Section III-B. The numerical stability can be regained by using either a mesh refinement scheme or an upwind procedure [9]–[11], whereas the former technique requires an unusually substantial expense in computer resources and the latter is accompanied with the disadvantage of a loss in accuracy [12]. Therefore, the numerical simulation of the motional eddy current phenomena is effective but complicated and time consuming.

On the other hand, the analytical calculation models with the advantages of a clear physical meaning, less computation time, and less computation resource requirements, are promising provided that they are sufficiently accurate. The PM eddy current devices with specific mechanical structures were described analytically in previous researches, where the eddy currents in the

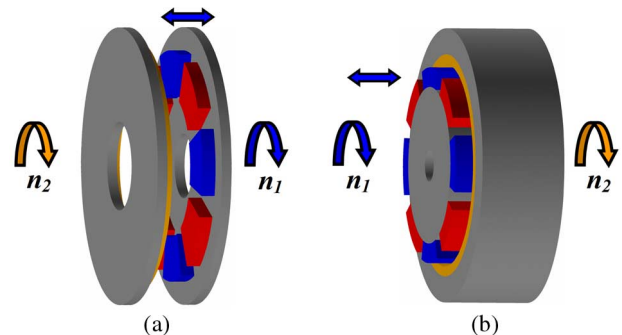


Fig. 1 PM eddy-current couplings: (a) axial flux type (disk type); (b) radial flux type (cylindrical type).

iron regions were ignored by applying infinite permeability or zero conductivity [13]–[17], or were considered by using an envisaged value of permeability [18]–[21]. Furthermore, the saturation effects occurring in the solid iron parts were omitted in all these calculation models.

The objective of this paper is to develop a general 2-D analytical formulation of the electromagnetic fields in eddy current couplings with regard to a frame of reference fixed to the conductor. The eddy current and saturation effects in the solid secondary back iron are taken into account. In addition, other common and unavoidable issues, such as the equivalent formulation for the PM blocks, the treatment of various PM shapes, are all rationally considered.

## II. THEORY

### A. Problem Description

The secondary unit of a PM eddy current coupling commonly adopts the two-layer structure composed of copper or aluminum and iron to combine their merits of high conductivity and high permeability and thus to produce the desirable torque characteristics. Since both the axial flux (i.e., disk type) and the radial flux (i.e., cylindrical type) eddy current couplings have the round shaped and geometric closed structure, the five-layer model as illustrated in Fig. 2 can be created by imagining that the coupling is cut radially and spread flat in the circumferential direction. The equivalent model with the linear geometrical structure is therefore periodic symmetric in the  $x$  direction and its length is determined by the number of pole pairs. If the transverse edge

Manuscript received February 04, 2013; revised May 02, 2013; accepted August 12, 2013. Date of publication August 21, 2013; date of current version December 23, 2013. Corresponding author: H. Lin (e-mail: hyling@seu.edu.cn).

Color versions of one or more of the figures in this paper are available online at <http://ieeexplore.ieee.org>.

Digital Object Identifier 10.1109/TMAG.2013.2279073

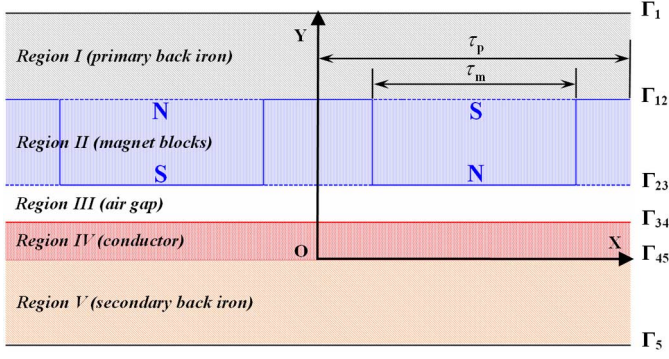


Fig. 2 Two-dimensional model of a PM eddy current coupling.

effects are temporarily ignored, i.e., the eddy currents are considered to flow only in the  $z$  direction, the actual 3-D problem is then reduced to a 2-D one.

Since there does not exist the relative motion between the magnetic field and the primary back iron, there are no saturation effects associated with eddy currents and skin effects in region I. The secondary back iron, on the contrary, is prone to magnetic saturation and the saturation phenomena would be intensified with the increasing relative velocity.

The main assumptions underlying the analytical model are as follows.

- 1) The five regions are composed of linear media.
- 2) The conductor and its back iron are “stationary,” and the magnet blocks and corresponding back iron are “moving” with the velocity  $v$ .
- 3) The permeability of primary back iron is the average permeability of iron material while that of secondary back iron is represented as an equivalent permeability to take into account the saturation behavior.
- 4) The thicknesses of two back iron layers are limited and the flux-parallel boundary condition is satisfied both on  $\Gamma_1$  and on  $\Gamma_5$ .

Based on the above assumptions, the motional conductor eddy current problem actually involving the nonlinear iron regions is further simplified to a linear problem and the boundary value problem can be outlined.

### B. Basic Governing Equation

In the field regions containing PMs, the constitutive relationship can be written as

$$\mathbf{B} = [\mu] \mathbf{H} + \mu_0 \mathbf{M}_e \quad (1)$$

where  $\mathbf{B}$  and  $\mathbf{H}$  are respectively the magnetic induction and the magnetic field intensity vectors,  $[\mu]$  and  $\mu_0$  are respectively the equivalent permeability tensor and the vacuum permeability, and  $\mathbf{M}_e$  is the effective remanent magnetization vector in the PM region.

By using the magnetic vector potential  $\mathbf{A}$  and taking the curl of (1), there is

$$\nabla \times \nabla \times \mathbf{A} = \nabla \times [\mu] \mathbf{H} + \nabla \times \mu_0 \mathbf{M}_e. \quad (2)$$

If material discontinuities are considered by using the interface continuity conditions, in every homogeneous region (2) can be rewritten as

$$\nabla \times \nabla \times \mathbf{A} = [\mu] \nabla \times \mathbf{H} + \mu_0 \nabla \times \mathbf{M}_e. \quad (3)$$

According to Ampere’s law, there is

$$\nabla \times \mathbf{H} = \mathbf{J} \quad (4)$$

where

$$\mathbf{J} = \sigma \left( -\frac{\partial \mathbf{A}}{\partial t} - \nabla \varphi + \mathbf{v} \times \nabla \times \mathbf{A} \right) \quad \text{for the 3-D case} \quad (5)$$

and

$$\begin{aligned} \mathbf{J} &= \sigma \left( -\frac{\partial \mathbf{A}}{\partial t} + \mathbf{v} \times \nabla \times \mathbf{A} \right) \quad \text{with} \\ \mathbf{A} &= A_z \mathbf{e}_z \quad \text{for the 2-D case} \end{aligned} \quad (6)$$

where  $\sigma$  is the material conductivity,  $\varphi$  is the electric scalar potential,  $\mathbf{v}$  is the relative velocity between the primary and the secondary and is measured in m/s, and  $\mathbf{e}_x$ ,  $\mathbf{e}_y$  and  $\mathbf{e}_z$  are the unit vectors in the  $x$ ,  $y$  and  $z$  directions, respectively. In a magnet frame of reference, the term  $\mathbf{v} \times \nabla \times \mathbf{A}$  (Lorentz term) comes from Minkowski transformation of the magnetic field in the moving conducting material, whereas the Lorentz term disappears in a conductor frame of reference. Thus the basic governing equation applicable to all the five linear regions depicted in Fig. 2 is derived as

$$\nabla \times \nabla \times \mathbf{A} = -[\mu] \sigma \frac{\partial \mathbf{A}}{\partial t} + \mu_0 \nabla \times \mathbf{M}_e. \quad (7)$$

### C. Formulation for the PM Region

The PM region in this paper is treated as the source of the traveling magnetic field, and in the Cartesian coordinates there is

$$\begin{aligned} \mathbf{M}_e &= M_y(x, t) \mathbf{e}_y \\ &= \sum_{n=1,3,5,\dots} \frac{4B_r}{\mu_0 n \pi} \sin \left( \frac{n \pi \tau_m}{2 \tau_p} \right) \cos(n s \omega_1 t - \alpha_n x) \mathbf{e}_y \end{aligned} \quad (8)$$

where  $B_r$  is the remanent induction of PMs,  $\tau_m$  and  $\tau_p$  are respectively the mean pole/pole-arc length and the pole pitch (see Fig. 2), the slip  $s$  and the electrical angular velocity of the primary  $\omega_1$  (rad/s) are respectively defined as

$$s = (n_1 - n_2)/n_1 \quad (9)$$

and

$$\omega_1 = 2 \pi n_1 p / 60 \quad (10)$$

and

$$\alpha_n = n \pi / \tau_p \quad (11)$$

$p$  being the number of pole pairs. The relationship between the magnitude of the relative velocity and the slip is

$$v = \omega_1 \tau_p s / \pi. \quad (12)$$

On the other hand, in the PM region there are

$$\nabla \times \nabla \times \mathbf{A} = \mu_0 \nabla \times \mathbf{M}_e \quad (13)$$

and

$$\mathbf{H} = [\mu]^{-1} (\mathbf{B} - \mu_0 \mathbf{M}_e) \quad (14)$$

with the equivalent permeability tensor

$$[\mu] = \begin{bmatrix} \mu_x & & \\ & \mu_y & \\ & & \mu_z \end{bmatrix}. \quad (15)$$

By collecting (8), (13), (14), and (15), and considering the present 2-D problem, an important relation is derived as

$$\mathbf{H} = \mu_x^{-1} B_x \mathbf{e}_x + \mu_y^{-1} (B_y - \mu_0 M_y) \mathbf{e}_y \quad (16)$$

which is essential to the determination of the interface conditions between the PM region and other regions. Moreover, as in the case of silicon steel laminations [22], [23],  $\mu_x$ ,  $\mu_y$  and  $\mu_z$  can be expressed as

$$\mu_x = \mu_0 \mu_r / (\tau_m / \tau_p + \mu_r (1 - \tau_m / \tau_p)) \quad (17)$$

and

$$\mu_y = \mu_z = \mu_0 (1 + (\mu_r - 1) \tau_m / \tau_p) \quad (18)$$

where  $\mu_r$  is the relative recoil permeability of PM. Equation (17) will also be used in the following interface conditions. It should be pointed out that the field results are sensitive to the values of  $\mu_r$  and  $\mu_x$  although they are just slightly larger than the vacuum permeability.

#### D. Treatment of Saturation Effects

The predicted peak flux density in the secondary back iron may reach either a very large and physically impossible value or a small value far below saturation if an inappropriate equivalent permeability of secondary back iron is applied. Some analytical examples will be shown in Section III-C. Therefore,  $\mu_{eq}$  should be carefully determined.

An average equivalent permeability is defined in this work. For an iron plate with thickness  $d$ , the equivalent permeability can be effectively worked out by solving the following equations:

$$\frac{8}{3\pi\delta_A} = \frac{1}{2\delta} \frac{\sinh 2d/\delta - \sin 2d/\delta}{\cosh 2d/\delta + \cos 2d/\delta} \quad \text{for } \delta_A < d \quad (19)$$

$$\begin{aligned} \frac{8}{3\pi\delta_A} & \left(1 - (1 - d^2/\delta_A^2)^{3/2}\right) \\ &= \frac{1}{2\delta} \frac{\sinh 2d/\delta - \sin 2d/\delta}{\cosh 2d/\delta + \cos 2d/\delta} \quad \text{for } \delta_A \geq d \end{aligned} \quad (20)$$

where

$$\delta_A = \sqrt{2H_o / (s\omega_1 c_s B_s \sigma_b)} \quad (21)$$

$$\delta = \sqrt{2 / (s\omega_1 \sigma_b \mu_{eq})} \quad (22)$$

and  $B_s$  is the peak magnetic flux density at the surface of back iron,  $H_o$  being the corresponding magnetic field intensity as obtained from the actual steel characteristics. The empirical coefficient  $c_s$  is set to 0.75, following Agarwal [24]. More details on the derivation of the calculation model are reported in Appendix A.

#### E. Analytical Solution of the Field Equations

Using the time-harmonic electromagnetic analysis, (8) can be rewritten in terms of the vector phasor as

$$\mathbf{M}_e(x, t) = \sum_{n=1,3,5,\dots} \text{Re} \left( \tilde{M}_n(x) e^{jn s \omega_1 t} \right) \mathbf{e}_y \quad (23)$$

with

$$\begin{aligned} \tilde{M}_n(x) &= M'_n e^{-j\alpha_n x} \\ &= \frac{4B_r}{\mu_0 n \pi} \sin \left( \frac{n \pi \tau_m}{2 \tau_p} \right) e^{-j\alpha_n x}. \end{aligned} \quad (24)$$

A tilde over a variable denotes its phasor form.

Thus a solution of the form is

$$\mathbf{A}(x, y, t) = \sum_{n=1,3,5,\dots} \text{Re} \left( \tilde{A}_{zn}(x, y) e^{jn s \omega_1 t} \right) \mathbf{e}_z \quad (25)$$

with

$$\tilde{A}_{zn}(x, y) = \tilde{A}'_{zn}(y) e^{-j\alpha_n x}. \quad (26)$$

If the  $n$ -th harmonic component is considered here, there are obviously  $\partial/\partial t = jn s \omega_1$  and  $\partial/\partial x = -j\alpha_n$ . Then the field equations associated with the  $n$ -th harmonic can be written in scalar form as

$$\frac{\partial^2 \tilde{A}_{zn}^{\text{I,III}}}{\partial y^2} - \alpha_n^2 \tilde{A}_{zn}^{\text{I,III}} = 0 \quad \text{in regions I and III} \quad (27)$$

$$\frac{\partial^2 \tilde{A}_{zn}^{\text{II}}}{\partial y^2} - \alpha_n^2 \tilde{A}_{zn}^{\text{II}} = j\mu_0 \alpha_n \tilde{M}_n \quad \text{in region II} \quad (28)$$

$$\frac{\partial^2 \tilde{A}_{zn}^{\text{IV}}}{\partial y^2} - (\alpha_n^2 - j\mu_0 \sigma_c n s \omega_1) \tilde{A}_{zn}^{\text{IV}} = 0 \quad \text{in region IV} \quad (29)$$

$$\frac{\partial^2 \tilde{A}_{zn}^{\text{V}}}{\partial y^2} - (\alpha_n^2 - j\mu_{eq} \sigma_b n s \omega_1) \tilde{A}_{zn}^{\text{V}} = 0 \quad \text{in region V} \quad (30)$$

where  $\sigma_c$  and  $\sigma_b$  are the conductivities of conductor and corresponding back iron, respectively.

The conductivity, an important parameter in determining the calculation results, is intimately associated with the working temperature. Furthermore, in order to accurately implement the experimental verification of the analytical model described in the following section, where the surface temperatures of the conductor and its back iron of the prototype were measured under various operating conditions, all the measured torques are separately related to different temperatures. Therefore, it is necessary to take account of the dependency of the conductivity on the working temperature. The relationship between the conductivity and the temperature  $\Theta$  can be expressed as

$$\sigma(\Theta) = \sigma_{20} (1 + \alpha \Theta_0) / (1 + \alpha \Theta) \quad (31)$$

where  $\sigma_{20}$  is the conductivity at 20°C,  $\Theta_0 = 20^\circ\text{C}$ ,  $\alpha = 0.004/^\circ\text{C}$  for copper and aluminum, and  $\alpha = 0.0056/^\circ\text{C}$  for iron.

The solutions are derived separately as

$$\tilde{A}_{zn}^{\text{I,III}} = (C_n^{\text{I,III}} e^{\alpha_n y} + D_n^{\text{I,III}} e^{-\alpha_n y}) e^{-j\alpha_n x} \quad (32)$$

$$\tilde{A}_{zn}^{\text{II}} = (C_n^{\text{II}} e^{\alpha_n y} + D_n^{\text{II}} e^{-\alpha_n y}) e^{-j\alpha_n x} - j\mu_0 \tilde{M}_n / \alpha_n \quad (33)$$

$$\tilde{A}_{zn}^{\text{IV}} = (C_n^{\text{IV}} e^{\beta_{cn} y} + D_n^{\text{IV}} e^{-\beta_{cn} y}) e^{-j\alpha_n x} \quad (34)$$

$$\tilde{A}_{zn}^{\text{V}} = (C_n^{\text{V}} e^{\beta_{bn} y} + D_n^{\text{V}} e^{-\beta_{bn} y}) e^{-j\alpha_n x} \quad (35)$$

where

$$\beta_{cn} = \sqrt{\alpha_n^2 - j\mu_0 \sigma_c n s \omega_1} \quad (36)$$

$$\beta_{bn} = \sqrt{\alpha_n^2 - j\mu_{eq} \sigma_b n s \omega_1}. \quad (37)$$

The boundary conditions to be satisfied are

$$\frac{\partial \tilde{A}_{zn}^{\text{I}}}{\partial x} = 0 \quad \text{on } \Gamma_1 \quad (38)$$

$$\frac{1}{\mu_x} \frac{\partial \tilde{A}_{zn}^{\text{II}}}{\partial y} = \frac{1}{\mu_{av}} \frac{\partial \tilde{A}_{zn}^{\text{I}}}{\partial y} \quad \text{and} \quad \frac{\partial \tilde{A}_{zn}^{\text{II}}}{\partial x} = \frac{\partial \tilde{A}_{zn}^{\text{I}}}{\partial x} \quad \text{on } \Gamma_{12} \quad (39)$$

$$\frac{1}{\mu_0} \frac{\partial \tilde{A}_{zn}^{\text{III}}}{\partial y} = \frac{1}{\mu_x} \frac{\partial \tilde{A}_{zn}^{\text{II}}}{\partial y} \quad \text{and} \quad \frac{\partial \tilde{A}_{zn}^{\text{III}}}{\partial x} = \frac{\partial \tilde{A}_{zn}^{\text{II}}}{\partial x} \quad \text{on } \Gamma_{23} \quad (40)$$

$$\frac{1}{\mu_0} \frac{\partial \tilde{A}_{zn}^{\text{IV}}}{\partial y} = \frac{1}{\mu_0} \frac{\partial \tilde{A}_{zn}^{\text{III}}}{\partial y} \quad \text{and} \quad \frac{\partial \tilde{A}_{zn}^{\text{IV}}}{\partial x} = \frac{\partial \tilde{A}_{zn}^{\text{III}}}{\partial x} \quad \text{on } \Gamma_{34} \quad (41)$$

$$\frac{1}{\mu_{eq}} \frac{\partial \tilde{A}_{zn}^{\text{V}}}{\partial y} = \frac{1}{\mu_0} \frac{\partial \tilde{A}_{zn}^{\text{IV}}}{\partial y} \quad \text{and} \quad \frac{\partial \tilde{A}_{zn}^{\text{V}}}{\partial x} = \frac{\partial \tilde{A}_{zn}^{\text{IV}}}{\partial x} \quad \text{on } \Gamma_{45} \quad (42)$$

$$\frac{\partial \tilde{A}_{zn}^{\text{V}}}{\partial x} = 0 \quad \text{on } \Gamma_5. \quad (43)$$

Substituting (32)-(35) into (38)-(43), ten linear equations are formed and can be expressed as

$$[\mathbf{K}]\{\mathbf{U}\} = \{\mathbf{R}\} \quad (44)$$

where  $[\mathbf{K}]$ ,  $\{\mathbf{R}\}$ , and  $\{\mathbf{U}\}$  are respectively the constant matrix, the constant column vector, and the unknown coefficient vector, their detailed forms being given in Appendix B. The vector  $\{\mathbf{U}\}$  can be easily found by using scientific computing environments such as Matlab, although the solutions for the coefficients are all in exceedingly lengthy form.

The magnetic induction and the current density vectors are obtained according to

$$\tilde{\mathbf{B}}_n = \tilde{\mathbf{B}}_{xn} + \tilde{\mathbf{B}}_{yn} = \frac{\partial \tilde{A}_{zn}}{\partial y} \mathbf{e}_x - \frac{\partial \tilde{A}_{zn}}{\partial x} \mathbf{e}_y \quad (45)$$

$$\tilde{\mathbf{J}}_n = -j\sigma n s \omega_1 \tilde{A}_{zn} \mathbf{e}_z. \quad (46)$$

Supposing that the magnetic field travels with the velocity  $v\mathbf{e}_x$ , the time-averaged traction force per unit width, taking all the pole pairs into consideration, is then calculated by

$$\begin{aligned} \mathbf{F}_{2D}^t &= p \sum_{n=1,3,5,\dots} \left( \int_{y_5}^{y_{34}} \int_{-\tau_p}^{\tau_p} \frac{1}{2} \text{Re} \left( \tilde{\mathbf{J}}_n^* \times \tilde{\mathbf{B}}_{yn} \right) dx dy \right) \\ &= \frac{\pi p \sigma s \omega_1}{2\tau_p} \sum_{n=1,3,5,\dots} \left( \int_{y_5}^{y_{34}} \int_{-\tau_p}^{\tau_p} n^2 |\tilde{A}_{zn}|^2 dx dy \right) \mathbf{e}_x \end{aligned} \quad (47)$$

where  $\tilde{\mathbf{J}}_n^*$  is the complex conjugate of  $\tilde{\mathbf{J}}_n$ ,  $y_5$  and  $y_{34}$  being the ordinates respectively corresponding to  $\Gamma_5$  and  $\Gamma_{34}$ . Equation (47) can be further simplified as

$$\mathbf{F}_{2D}^t = \pi p \sigma s \omega_1 \sum_{n=1,3,5,\dots} n^2 \left( \int_{y_5}^{y_{34}} |\tilde{A}_{zn}'|^2 dy \right) \mathbf{e}_x. \quad (48)$$

Reference [25] presented a correction factor which was derived from the ratio of the eddy current loss associated with a 2-D current distribution to that due to a 1-D current field (i.e., the power loss calculated by disregarding the transverse edge effects), in the screened-rotor induction motor. The correction factor  $k_s$  is adopted here to account for the real eddy current path and the actual coupling geometry

$$k_s = 1 - \frac{\tanh \lambda_m}{\lambda_m (1 + \tanh \lambda_m \tanh \lambda_{cm})} \quad (49)$$

where

$$\lambda_m = \pi w_m / (2\tau_p) \quad (50)$$

$$\lambda_{cm} = \pi (w_c - w_m) / (2\tau_p) \quad (51)$$

where  $w_c$  is the conductor width in the  $z$  direction,  $w_m$  being the width of overlapping area between the magnets and the conductor. The correction factor was widely introduced to the eddy current field calculations in electromagnetic machines to rationalize the calculation results of 2-D fields [14], [26], [27].

Since the eddy current loss and the electromagnetic force are all associated with  $|\tilde{A}_{zn}|^2$ , the force can be rewritten in the same way as the case of the power loss to allow for the transverse edge effects. The modified attraction force is thus expressed as

$$\mathbf{F}_{3D}^t = k_s w_m \mathbf{F}_{2D}^t. \quad (52)$$

The transmission torque is further calculated by

$$T = |\mathbf{r}_{mean} \times \mathbf{F}_{3D}^t| \quad (53)$$

where  $\mathbf{r}_{mean}$  is the mean moment arm. The output power produced by all the pole pairs is obtained simultaneously as

$$P_2 = \omega_1 (1 - s) T / p. \quad (54)$$

#### F. Equivalence Relationships between Typical PM Shapes

Up to this point, there is still an undetermined aspect for a complete theory of eddy current couplings. PM shapes related to the widely applied axial flux (i.e., disk type) couplings are diverse. Since the values of pole/pole-arc length and pole pitch are all dependent on the PM shapes, the PM geometry should be sensibly converted in the proposed 2-D analytical model where only the rectangular-shaped magnet is desirable. The permanent

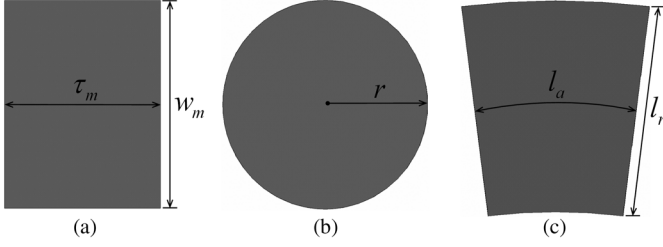


Fig. 3 Common types of permanent magnets used in couplings: (a) rectangular-shaped; (b) circular-shaped; (c) fan-shaped.

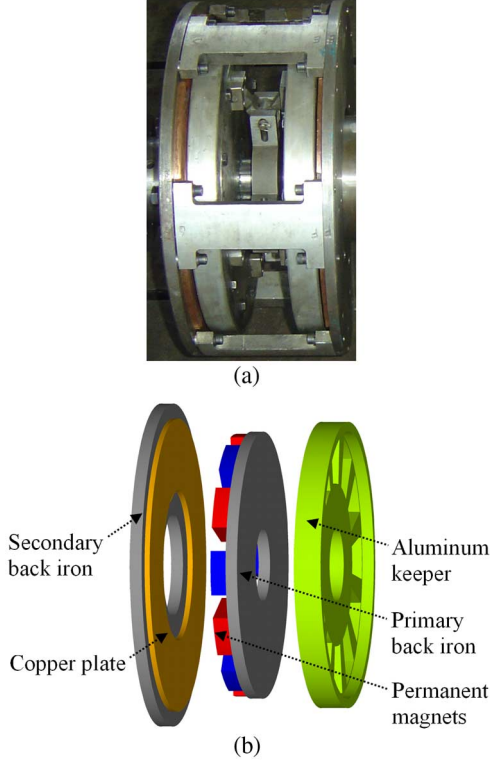


Fig. 4 Axial flux eddy-current coupling: (a) prototype (symmetric structure); (b) mechanical schematic (single side).

magnets with other shapes, such as circular-shaped and fan-shaped magnets, should all be equalized to the corresponding rectangular-shaped one with the same area and thickness. The equivalence principle, which can be easily verified by using 3-D finite element method, first appeared in the research literature [28], and will be extended to the general case in this paper.

The main relationship between the magnets with typical profiles is illustrated in Fig. 3. The associated conditions for the circular-shaped magnet are

$$r = \sqrt{\tau_m w_m / \pi} \quad (55)$$

and

$$\tau_m = w_m \quad (56)$$

from which the size of matching rectangular-shaped magnet, i.e.,  $\tau_m$  and  $w_m$ , can be found. For the fan-shaped magnet the radial length  $l_r$  can be set to  $w_m$ , and then its average arc length  $l_a$  is easily found to equal  $\tau_m$ . As for magnets of other shapes, the similar correspondence principle is also applicable.

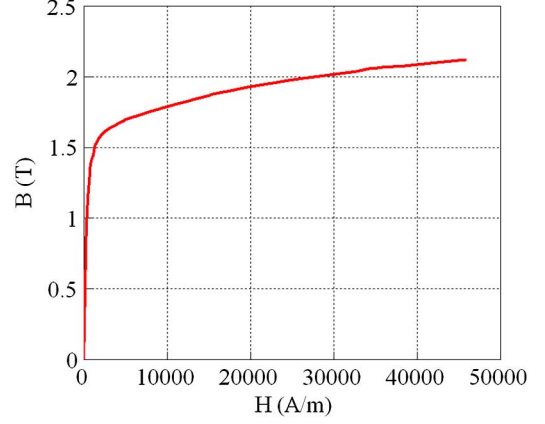


Fig. 5 B-H curve for the ferromagnetic material.

TABLE I  
SPECIFICATIONS OF THE PROTOTYPE EDDY CURRENT COUPLING

Parameter	Symbol	Value	Unit
Number of pole pairs	$p$	6	-
Mean pole-arc length	$\tau_m$	0.0468	m
Mean pole pitch	$\tau_p$	0.072	m
Magnet thickness	-	0.02	m
Width of the overlapping area	$w_m$	0.065	m
Copper plate width	$w_c$	0.09	m
Copper plate thickness	-	0.0065	m
Mean moment arm	$r_{mean}$	0.1375	m
Primary back iron thickness	-	0.015	m
Secondary back iron thickness	$d$	0.015	m
Rotation speed of the primary	$n_1$	$1495 \pm 5$	rpm
Copper conductivity (20 °C)	$\sigma_c$	57.1	MS/m
Iron conductivity (20 °C)	$\sigma_b$	6.9	MS/m

### III. MODEL VERIFICATION

#### A. Coupling Prototype

A 75 kW prototype with the double-sided structure, as shown in Fig. 4, was built where the fan-shaped NdFeB magnets (remanent induction 1.21 T, relative recoil permeability 1.099) were mounted in two aluminum keepers. The design and material parameters are given in Table I. Furthermore, the nonlinear magnetic property for the primary and secondary back irons is shown in Fig. 5, from which the average permeability is obtained as  $\mu_{av} = 1346 \mu_0$ . The slip  $s$  and the air gap length  $g$  are all controllable variables.

#### B. Comparison with Nonlinear FEA Results

The prototype under two typical operating conditions is investigated and the results are reported in Figs. 6 and 7. The influences of the eddy current and the air gap reluctance on the magnetic field are well demonstrated. The predicted air gap flux density distributions by the proposed analytical model are compared with those obtained from the 2-D nonlinear finite element analysis (FEA). The FE calculation is conducted with the same geometric model as the analytical one but using the magnetization curve instead of the equivalent permeability to describe the saturation behavior. The Peclet number  $Pe = \sigma \mu v L / 2$  where  $L$  is the element length in the motion direction, should be smaller than unity in the numerical calculation of moving eddy current



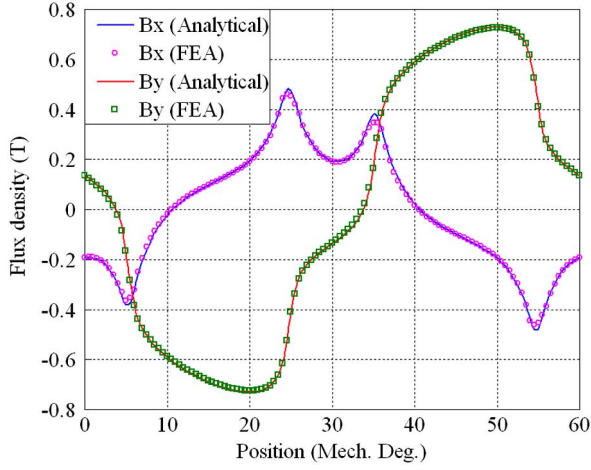


Fig. 6 Magnetic field distribution in the middle of the air gap ( $g = 4$  mm,  $s = 0.02$ ,  $\mu_{eq} = 106 \mu_0$ ).

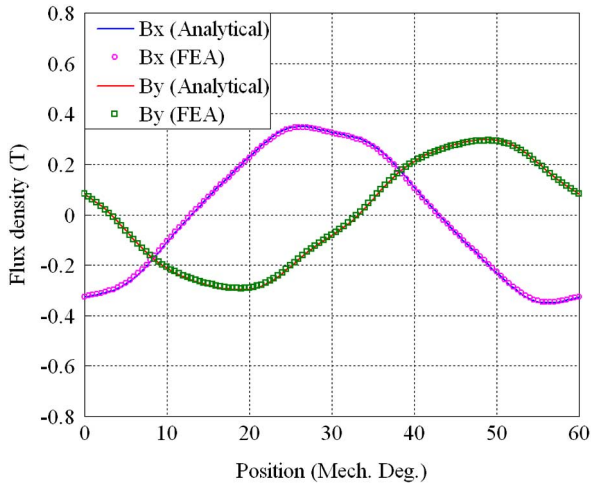


Fig. 7 Magnetic field distribution in the middle of the air gap ( $g = 23$  mm,  $s = 0.16$ ,  $\mu_{eq} = 209 \mu_0$ ).

problems. Therefore, a sufficiently fine mesh is generated to retain numerical stability.

As shown in Figs. 6 and 7, excellent agreement is observed. The deviations between the analytical and FEA results are, in general, below 2%, while the large deviations appear in the vicinity of  $B_x$  or  $B_y = 0$  where the flux density values are very small. Two preliminary conclusions, therefore, can be drawn from the comparison results. On the one hand, since the FE model takes into account the actual complexity of the magnet geometry, the formulation of magnetic property of PM region in the proposed analytical model proves to be valid and practical. On the other hand, the approximate treatment of the iron nonlinearity by using the average equivalent permeability can obtain the same magnetic flux distributions in the air gap as the nonlinear calculation using the B-H curve. The above two conclusions will be further examined in the following sub-sections. The comparison results also indicate that the presented model can legitimately replace the nonlinear numerical method with the same accuracy but with less computation cost.

TABLE II  
CALCULATED PEAK FLUX DENSITIES WITH THE DIFFERENT EQUIVALENT PERMEABILITIES OF SECONDARY BACK IRON

Air gap (mm)	Slip	$\mu_{eq}$	$B_s$ (T)
4	0.02	$30 \mu_0$	1.21
		$106 \mu_0$ (calculated from (20))	1.98
		$300 \mu_0$	3.60
23	0.16	$60 \mu_0$	1.03
		$209 \mu_0$ (calculated from (19))	1.97
		$600 \mu_0$	3.38

TABLE III  
CALCULATED TOTAL TORQUES WITH THE DIFFERENT FORMULATIONS OF MAGNETIC PROPERTY OF PM REGION

Air gap (mm)	Slip	$\mu_s$	$T$ (Nm)	
			Analytical	FEA
4	0.02	defined by (17)	369	370
		$\mu_0$	388	
		$\mu_0 \mu_r$	358	
23	0.16	defined by (17)	162	161
		$\mu_0$	175	
		$\mu_0 \mu_r$	156	

### C. Influence of the Expressions for the Magnetic Properties on Field Results

Table II demonstrates that either the larger or the smaller values of the permeability of secondary back iron would yield physically unreasonable results. The reason behind this phenomenon is the skin effect. A larger permeability would bring about a smaller skin depth where most of the magnetic flux passes through, thus resulting in an abnormally large peak flux density. In the case of a smaller permeability, the opposite effect would be observed. Only with the appropriate value of  $\mu_{eq}$  can the correct field results be obtained.

In Table III, two formulations of magnetic property of PM region which are commonly found in literature and the expression used in the proposed analytical model are investigated and the analytically calculated torques are compared to the FEA results. It is clearly shown that the proposed formulation for the PM region is practical and accurate.

### D. Harmonic Spectrum of the Calculated Torque

A typical frequency spectrum of the analytically calculated torques is exhibited in Fig. 8. It can be observed that the fundamental harmonic component plays a dominant role in the torque transmission system while the second largest harmonic component, i.e., 5th harmonic, contributes to only about 0.3% of the total torque. Therefore, in the analytical model the satisfactory calculation accuracy can be achieved when just the first several harmonic orders are chosen.

On the other hand, Fig. 8 also shows that the eddy currents and then the electromagnetic forces associated with the secondary back iron are small compared to those related to the copper region, but they should not be omitted. In the case shown in Fig. 8, the iron region accounts for 7.29% of the total torque.

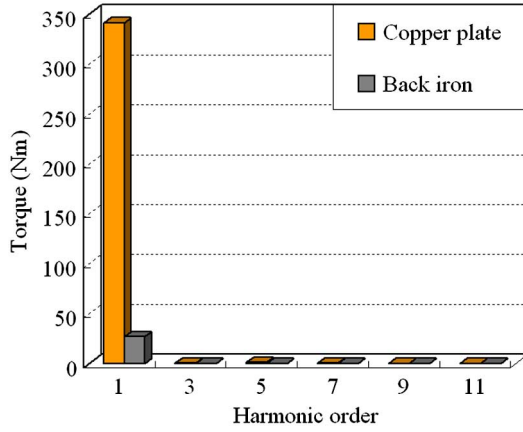


Fig. 8 Harmonic spectrum of the analytically calculated torques ( $g = 4$  mm,  $s = 0.02$ ,  $\mu_{eq} = 106 \mu_0$ ).

### E. Comparison with Test Results

An experimental setup was constructed. The primary of the prototype machine was connected to an asynchronous motor while the secondary unit was coupled, via a torque sensor, to an electric eddy current dynamometer used as a controlled load. A handheld speedometer was used to acquire the rotation speeds of the primary and secondary units. The surface temperatures of the conductor and its back iron were measured by means of an infrared thermometer. A set of measurements for different air gap lengths and slips were conducted.

For the axial flux eddy current coupling, there are, in addition to the aforementioned traction force (i.e., tangent force) acting on the secondary, also both a repulsive force and an attraction force (i.e., two normal forces) between the primary and the secondary. It is found that, with growing slip speed, the repulsive force will continue to increase while the attraction force will keep dropping. The repulsive force will become dominant as the slip reaches a certain critical value, and then there is such a tendency that the net repulsive force makes the air gap larger. Therefore, in order to rationally handle the experimental set-up, the small air gaps were limited to the cases of the small slips, and the slip was adjusted over a wider range when the air gap was set to a larger value. The largest slip related to the maximum air gap length 23 mm was regulated to approximately 0.16.

The cases of the minimum and the maximum air gaps are chosen here to evaluate the effectiveness of the proposed analytical model. In Figs. 9 and 10, a comparison of the analytically predicted torque-slip characteristics with the nonlinear FEA results and the measured data is illustrated. In order to show the general trend in torque variation, in Fig. 10, the analytical and FE predictions over a wider range of slip values (larger than 0.16) are given. After the initial increase, the predicted torque, as demonstrated in Fig. 10, begins to drop with the growing slip. The reason for this phenomenon is that the magnetic field weakening caused by the eddy currents induced in the secondary units becomes severe at high slips.

As can be seen from Figs. 9 and 10, the analytical results are still almost identical to the nonlinear FEA ones. The analytical predictions are also very close to the experimental measurements in the case of the small air gap. As the air gap becomes larger, however, the deviations between the calculated results and the measured ones begin to increase. A possible explanation

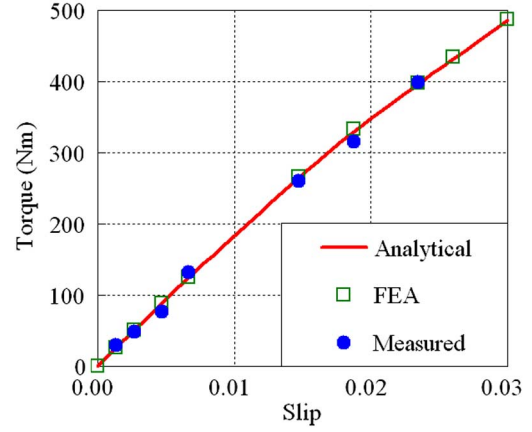


Fig. 9 Analytical, 2-D nonlinear FEA, and experimental results of torque values ( $g = 4$  mm).

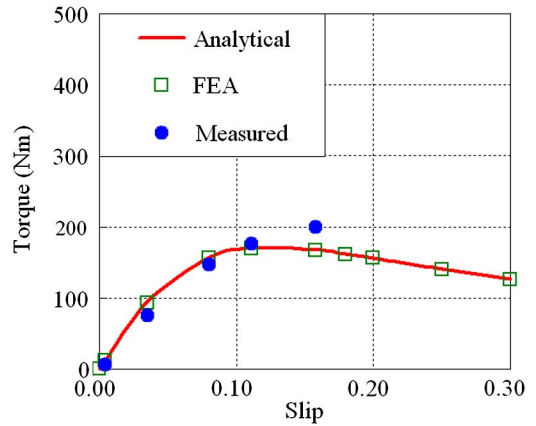


Fig. 10 Analytical, 2-D nonlinear FEA, and experimental results of torque values ( $g = 23$  mm).

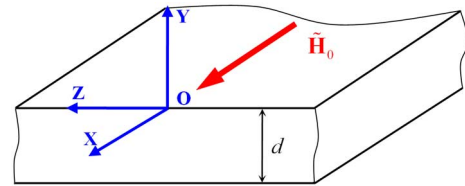


Fig. 11 Ferromagnetic plate with a sinusoidal excitation applied to its surface.

for this phenomenon is the actual existence of the  $z$  component of the magnetic field which would become comparable to the  $x$  and  $y$  components when the air gap expands. In the cases of large air gaps, the  $y$  component of the magnetic field in a 2-D model is, therefore, larger than that in the real 3-D problem when the slip is small and the magnetic field reduction due to the eddy currents is insignificant. As the slip becomes greater, on the contrary,  $B_y$  undergoes a more severe weakening in a 2-D problem than in the actual 3-D case. Therefore, the measured torque at high slips is larger than the predicted value.

In practical applications, eddy current couplings normally operate at as small an air gap as can be reasonably maintained and the cases of large air gaps just occur in the transient stages, such as the starting and braking stages. It can be concluded, therefore, that the proposed analytical technique can effectively determine the steady state torque characteristics of PM eddy current couplings and it can also validly predict the general trends for the torque behaviors in the starting and braking stages.





Technology Support Project (BY2011151), and the Senior Expert Special Foundation in 6 Fields of Jiangsu Province of China (2011-ZBZZ-016).

# REFERENCES

- [1] D. Alibert, S. Dappen, and G. Henneberger, "Calculation of the 3D non-linear eddy current field in moving conductors and its application to braking systems," *IEEE Trans. Magn.*, vol. 32, no. 3, pp. 768–771, May 1996.
- [2] A. C. Smith, H. Willsamson, N. Benhama, L. Counter, and J. M. Papadopoulos, "Magnetic drive couplings," in *Proc. IEE Electr. Mach. and Drives Conf.*, 1999, pp. 232–236.
- [3] K. Atallah and J. Wang, "A brushless permanent magnet machine with integrated differential," *IEEE Trans. Magn.*, vol. 47, no. 10, pp. 4246–4249, Oct. 2011.
- [4] L. Z. Ye, D. S. Li, Y. J. Ma, and B. F. Jiao, "Design and performance of a water-cooled permanent magnet retarder for heavy vehicles," *IEEE Trans. Energy Convers.*, vol. 26, no. 3, pp. 953–958, Sep. 2011.
- [5] T. W. Nehl, B. Lequesne, V. Gangla, S. A. Gutkowski, M. J. Robinson, and T. Sebastian, "Nonlinear two-dimensional finite element modeling of permanent magnet eddy current couplings and brakes," *IEEE Trans. Magn.*, vol. 30, no. 5, pp. 3000–3003, Sep. 1994.
- [6] H. K. Razavi and M. U. Lampérth, "Eddy-current coupling with slotted conductor disk," *IEEE Trans. Magn.*, vol. 42, no. 3, pp. 405–410, Mar. 2006.
- [7] N. Allen, D. Rodger, P. Coles, S. Street, and P. Leonard, "Towards increased speed computations in 3D moving eddy current finite element modelling," *IEEE Trans. Magn.*, vol. 31, no. 6, pp. 3524–3526, Nov. 1995.
- [8] S. E. Gay and M. Ehsani, "Parametric analysis of eddy-current brake performance by 3-D finite-element analysis," *IEEE Trans. Magn.*, vol. 42, no. 2, pp. 319–328, Feb. 2006.
- [9] M. Ziolkowski and H. Brauer, "Fast computation technique of forces acting on moving permanent magnet," *IEEE Trans. Magn.*, vol. 46, no. 8, pp. 2927–2930, Aug. 2010.
- [10] F. Henrotte, H. Heumann, E. Lange, and K. Hameyer, "Upwind 3-D vector potential formulation for electromagnetic braking simulations," *IEEE Trans. Magn.*, vol. 46, no. 8, pp. 2835–2838, Aug. 2010.
- [11] Y. P. Zhao, X. Zhang, S. L. Ho, and W. N. Fu, "A local discontinuous Galerkin method for eddy current field analysis in high-speed moving conductors," *IEEE Trans. Magn.*, vol. 48, no. 2, pp. 251–254, Feb. 2012.
- [12] K. C. Chan and S. Williamson, "Factors influencing the need for upwinding in two-dimensional field calculation," *IEEE Trans. Magn.*, vol. 28, no. 2, pp. 1611–1614, Mar. 1992.
- [13] R. B. Zmood, "Motional eddy currents in a nonmagnetic conducting laminate backed with an iron substrate," *J. Appl. Phys.*, vol. 57, no. 1, pp. 3860–3862, Apr. 1985.
- [14] J. D. Edwards, B. V. Jayawant, W. R. C. Dawson, and D. T. Wright, "Permanent-magnet linear eddy-current brake with a nonmagnetic reaction plate," *Proc. IEE*, vol. 146, no. 6, pp. 627–631, Nov. 1999.
- [15] A. Canova and B. Vusini, "Analytical modeling of rotating eddy-current couplers," *IEEE Trans. Magn.*, vol. 41, no. 1, pp. 24–35, Jan. 2005.
- [16] J. Y. Choi and S. M. Jang, "Analytical magnetic torque calculations and experimental testing of radial flux permanent magnet-type eddy current brakes," *J. Appl. Phys.*, vol. 111, no. 7, pp. 07E712–07E712-3, Apr. 2012.
- [17] A. Rahideh and T. Korakianitis, "Analytical armature reaction field distribution of slotless brushless machines with inset permanent magnets," *IEEE Trans. Magn.*, vol. 48, no. 7, pp. 2178–2191, Jul. 2012.
- [18] E. J. Davies, M. T. Wright, and H. McKibbin, "Three-dimensional theory of eddy-current couplings with copper-faced loss drums," *Proc. IEE*, vol. 124, no. 12, pp. 1187–1196, Dec. 1977.
- [19] M. Markovic and Y. Perriard, "An analytical determination of eddy-current losses in a configuration with a rotating permanent magnet," *IEEE Trans. Magn.*, vol. 43, no. 8, pp. 3380–3386, Aug. 2007.
- [20] P.-D. Pfister and Y. Perriard, "Slotless permanent-magnet machines: General analytical magnetic field calculation," *IEEE Trans. Magn.*, vol. 47, no. 6, pp. 1739–1752, Jun. 2011.
- [21] S. Sharif, J. Faiz, and K. Sharif, "Performance analysis of a cylindrical eddy current brake," *IET Electr. Power Appl.*, vol. 6, no. 9, pp. 661–668, Nov. 2012.
- [22] C. J. Carpenter, "Theory of flux penetration into laminated iron and associated losses," *Proc. IEE*, vol. 124, no. 7, pp. 659–664, Jul. 1977.
- [23] J. Wang, H. Y. Lin, Y. K. Huang, and X. K. Sun, "A new formulation of anisotropic equivalent conductivity in laminations," *IEEE Trans. Magn.*, vol. 47, no. 5, pp. 1378–1381, May 2011.
- [24] P. D. Agarwal, "Eddy-current losses in solid and laminated iron," *Trans. AIEE*, vol. 78, pt. Part I, pp. 169–181, May 1959.
- [25] R. L. Russell and K. H. Norsworthy, "Eddy currents and wall losses in screened-rotor induction motors," *Proc. IEE*, vol. 105, no. 20, pp. 163–175, Apr. 1958.
- [26] F. Eastham, T. Cox, P. Leonard, and J. Proverbs, "Linear induction motors with modular winding primaries and wound rotor secondaries," *IEEE Trans. Magn.*, vol. 44, no. 11, pp. 4033–4036, Nov. 2008.
- [27] P. Warberger, R. Kaelin, T. Nussbaumer, and J. W. Kolar, "50 N · m/2500 W bearingless motor for high-purity pharmaceutical mixing," *IEEE Trans. Ind. Electron.*, vol. 59, no. 5, pp. 2236–2247, May 2012.
- [28] K. Venkataratnam and D. Ramachandra Raju, "Analysis of eddy-current brakes with nonmagnetic rotors," *Proc. IEE*, vol. 124, no. 1, pp. 67–71, Jan. 1977.
- [29] O. Biro and K. Preis, "On the use of the magnetic vector potential in the finite-element analysis of three-dimensional eddy currents," *IEEE Trans. Magn.*, vol. 25, no. 4, pp. 3145–3159, Jul. 1989.

**Jian Wang** received the M.S. degree in electrical engineering from Hohai University, Nanjing, China, in 2003. Since 2009, he has been working toward the Ph.D. degree in electrical engineering at Southeast University, Nanjing, China.

Since 2003, he has been with Nanjing Institute of Technology, where he is now a Lecturer in the School of Automation. His research and teaching interests focus on the analysis and design of electromagnetic systems with an emphasis on eddy current problems in electrical machines and transformers.

**Heyun Lin** received the B.S., M.S., and Ph.D. degrees in electrical engineering from Nanjing University of Aeronautics and Astronautics, Nanjing, China, in 1985, 1989, and 1992, respectively.

From 1992 to 1994, he was a Postdoctoral Fellow at Southeast University, Nanjing, China. In 1994, he joined the School of Electrical Engineering, Southeast University, as an Associate Professor. He became a Full Professor in 2000. His main research is related to the design, analysis, and control of permanent-magnet motors, intelligent electrical apparatus, and electromagnetic field numerical analysis. He is the author of more than 60 technical papers and holder of ten patents.

**Shuhua Fang** received the M.S. degree from Shandong University of Science and Technology, Jinan, China, in 2004, and the Ph.D. degree from Southeast University, Nanjing, China, in 2008, both in electrical engineering.

From 1998 to 2001, he was an Associate Engineer with the Xuzhou Coal and Mine Machinery Factory, where his research activities were primarily in the area of the design, analysis, and control of electrical apparatus for coal and mines. He joined the School of Electrical Engineering, Southeast University, in 2008, where he is now an associate professor. His research interests include intelligent apparatus design, simulation, and control.

**Yunkai Huang** received the B.S., M.S., and Ph.D. degrees in electrical engineering from Southeast University, Nanjing, China, in 1998, 2001, and 2007, respectively.

Since 2001, he has been with Southeast University, where he is now an associate professor in the School of Electrical Engineering. His research interests focus on the design, analysis, and control of electrical machines.